Energy & Environmental Science



COMMUNICATION

View Article Online



Cite this: Energy Environ. Sci., 2023, 16, 3753

Received 8th May 2023, Accepted 31st July 2023

DOI: 10.1039/d3ee01450a

rsc li/ees

A giant Nernst power factor and figure-of-merit in polycrystalline NbSb₂ for Ettingshausen refrigeration†

Peng Li, ab Pengfei Qiu, *abc Jie Xiao, a Tingting Deng, c Lidong Chen ab and

Ettingshausen refrigeration is a promising solid-state refrigeration technology that can be used in exploring the quantum state of matters and superconducting materials, but its development is greatly limited by the lack of high-performance polycrystalline thermomagnetic materials. In this work, we report that the polycrystalline topological semimetal NbSb2 has a giant Nernst power factor ((PF)_N) of 1269 \times 10⁻⁴ W m⁻¹ K⁻² under 9 T at 28 K and a Nernst figure-of-merit (z_N) of 28.5 \times 10⁻⁴ K⁻¹ under 9 T at 18 K, both of which are record-high values among the polycrystalline thermomagnetic materials. The observed high thermomagnetic performance is mainly attributed to the large and unsaturated Nernst thermopower under a high magnetic field. Due to the diminished anisotropy, the polycrystalline NbSb2 has similar high carrier mobility to the single-crystalline NbSb2 in the bc-plane, yielding large Nernst thermopower in low temperature ranges. Combining the excellent thermomagnetic performance and lowcost and time-saving fabrication process, polycrystalline NbSb2 is a very competitive candidate material for Ettingshausen refrigeration.

Broader context

The demand for thermoelectric applications at low temperatures is heightened now by the exploration of quantum state of matters, quantum information science, and space science. However, today good thermoelectric and thermomagnetic materials in the low temperature range, particularly at temperatures below the liquid nitrogen boiling point, are still very rare. Discovering high performance thermoelectric and thermomagnetic materials below the liquid nitrogen temperature has become a very active field worldwide. In this work, we demonstrate that polycrystalline $NbSb_2$ has a giant Nernst power factor of $1269 \times 10^{-4} \text{ W m}^{-1} \text{ K}^{-2}$ under 9 T at 28 K and a Nernst figure-of-merit of 28.5 \times 10 $^{-4}$ K $^{-1}$ under 9 T at 18 K. These values are not only the highest among the polycrystalline thermomagnetic materials, but are also superior to many single-crystalline thermomagnetic materials reported before. More importantly, polycrystalline NbSb2 can be easily synthesized by using a low-cost and time-saving fabrication process, which is more competitive than the single-crystalline thermomagnetic materials for the fabrication of an Ettingshausen refrigerator. This work provides a new optional material for solid-state heat pumping below liquid nitrogen temperature based on Ettingshausen refrigeration.

Introduction

A low-temperature environment is essential for the investigation of quantum states of matter, superconducting materials, and space science.3 Beyond the traditional compressor refrigerator based on gaseous working substances, thermoelectric (TE) refrigeration provides an alternative way to obtain a low-temperature environment. 4-7 When a current flows through the thermoelectric (TE) device, the temperature at one end of the device can be reduced. According to the working principle, TE refrigeration can be divided into two categories, termed as Peltier refrigeration and Ettingshausen refrigeration. Besides the electric current, the latter one also needs the assistance of a magnetic field.

Compared with Peltier refrigeration, which has already realized commercialization several decades before, 4,5 the development of Ettingshausen refrigeration is relatively slow. The main reason is the lack of high performance thermomagnetic materials with a high Nernst power factor $((PF)_N = S_{\nu x}^2 \sigma_{\nu \nu})$ determining the transverse pumping power, where S_{yx} is the Nernst thermopower and σ_{yy} is the longitudinal electrical conductivity) and large Nernst figure-of-merit ($z_N = S_{yx}^2 \sigma_{yy} / \kappa_{xx}$, determining the maximum temperature gradient that can be built across the device, where κ_{xx} is the transverse thermal conductivity). To maximize $(PF)_N$ and z_N , the material for Ettingshausen refrigeration requires electrons and holes possessing

^a State Key Laboratory of High Performance Ceramics and Superfine Microstructure, Shanghai Institute of Ceramics, Chinese Academy of Science, Shanghai 200050, China. E-mail: qiupf@mail.sic.ac.cn, xshi@mail.sic.ac.cn

^b Center of Materials Science and Optoelectronics Engineering, University of Chinese Academy of Sciences, Beijing 100049, China

^c School of Chemistry and Materials Science, Hangzhou Institute for Advanced Study, University of Chinese Academy of Sciences, Hangzhou 310024, China

[†] Electronic supplementary information (ESI) available. See DOI: https://doi.org/

nearly identical concentrations and high mobilities, which greatly limit the scope of optional materials. Thus, for a long time, the investigation of Ettingshausen refrigeration was limited in a few thermomagnetic materials (e.g. Bi–Sb alloys 10,11 and In–Sb alloys 12). The peak (PF)_N and $z_{\rm N}$ are about 324 \times 10 $^{-4}$ W m $^{-1}$ K $^{-2}$ and 55 \times 10 $^{-4}$ K $^{-1}$ for single-crystalline Bi $_{97}$ Sb $_3$ under 1 T at 115 K, respectively. 10

Recently, the investigation of Ettingshausen refrigeration was rejuvenated due to the great progress achieved in topological semimetals. 13-15 A series of topological semimetals have been reported with high thermomagnetic performance, such as Cd₃As₂, ¹⁶ ZrTe₅, ¹⁷ PtSn₄, ¹⁸ Mg₂Pb, ¹⁹ NbSb₂, ²⁰ and WTe₂. ²¹ Some of them exhibit superior (PF)_N to the Bi-Sb alloys, such as 425 \times 10⁻⁴ W m⁻¹ K⁻² for single-crystalline Mg₂Pb under 10 T at 30 K, 19 3800 \times 10⁻⁴ W m⁻¹ K⁻² for single-crystalline NbSb₂ under 5 T at 25 K,²⁰ and 3 W m⁻¹ K⁻² for single-crystalline WTe₂ under 9 T at 11.3 K.²¹ The maximum z_N of thermomagnetic materials was boosted up to $265 \times 10^{-4} \, \text{K}^{-1}$ for single-crystalline WTe₂ under 9 T at 11.3 K.²¹ However, all these high (*PF*)_N and z_N are achieved in single crystals, in which the preparation methods are usually time-consuming and expensive. Furthermore, the crystal sizes are usually small, which greatly limit the real application of Ettingshausen refrigeration. In contrast to single crystals, the polycrystals can be easily prepared into large bulks by using simple and low-cost preparation methods, which are more suitable for real application. However, currently the investigation on polycrystalline thermomagnetic materials is very rare.^{22–25} Particularly, as shown in Fig. 1, the $(PF)_N$ and z_N of the reported polycrystalline thermomagnetic materials are much lower than those of single-crystalline thermomagnetic materials. Discovering the polycrystalline thermomagnetic materials with high (PF)_N and $z_{\rm N}$ has already become an important task for the investigation of Ettingshausen refrigeration.

In this work, we report the discovery of a colossal $(PF)_N$ of 1269×10^{-4} W m⁻¹ K⁻² under 9 T at 28 K and a high z_N of 28.5×10^{-4} K⁻¹ under 9 T at 18 K in polycrystalline NbSb₂, both of which are record-high values in polycrystalline thermomagnetic materials (Fig. 1). The excellent performance of polycrystalline NbSb₂ is caused by the nearly identical electron and hole concentrations near the Fermi level, ultrahigh mobilities close to 1 m² V⁻¹ s⁻¹, and a strong phonon-drag effect in low temperature ranges. This work provides a novel potential candidate material for Ettingshausen refrigeration.

Results and discussion

Polycrystalline NbSb₂ was fabricated by using the solid-state reaction and spark plasma sintering technique. Fig. 2a shows the powder X-ray diffraction pattern of polycrystalline NbSb₂. All diffraction peaks can be indexed belonging to the centrosymmetric monoclinic structure (space group C_2/m) of NbSb₂ (the inset in Fig. 2a). Backscattered electron (BSE) image (Fig. 2b) and energy dispersive X-ray spectroscopy (EDS) mapping (Fig. 2c and d) indicate that Nb and Sb are homogeneously distributed inside the matrix, confirming that the prepared

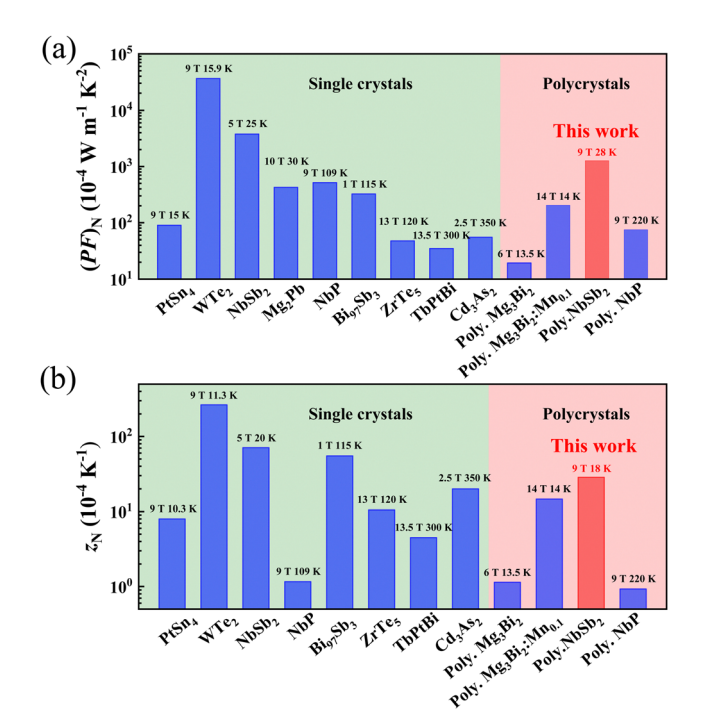


Fig. 1 (a) Comparisons of the (a) Nernst power factor $(PF)_N$ and (b) Nernst figure-of-merit z_N of polycrystalline NbSb₂ and some typical thermomagnetic materials reported before. $^{10,16-21,23-28}$ The maximum $(PF)_N$ and z_N of each thermomagnetic material are used in the figures.

polycrystalline $NbSb_2$ is phase pure. Fig. 2e shows that the grain sizes are about several micrometers. No obvious orientation is observed. Such high homogeneity and isotropy provide the basis for the accurate measurement of thermomagnetic performance in this work.

Fig. 3a shows the temperature dependence of the Seebeck thermopower S_{xx} of polycrystalline NbSb₂ under different magnetic fields B. In the absence of a magnetic field, the S_{xx} of polycrystalline NbSb₂ below 100 K is almost zero. This is consistent with the band structure of NbSb₂, with the schematics shown in the inset of Fig. 3a. The Fermi level crosses both the valence and conduction bands, demonstrating a typical feature of semimetals. Above 100 K, the S_{xx} decreases linearly with increasing temperature, reaching $-20~\mu V~K^{-1}$ at 300 K. When the magnetic field is applied, the S_{xx} below 100 K is significantly enhanced, while that above 100 K is only slightly increased. Similar temperature-dependence and magnetic field-dependence have been also observed in single-crystalline NbSb₂, indicating that the grain boundary has little influence on the S_{xx} .

Fig. 3b shows the temperature dependence of the Nernst thermopower S_{yx} of polycrystalline NbSb₂ under different magnetic fields B. Under each magnetic field, the absolute value of S_{yx} firstly increases with the increase of temperature, reaching a peak around 21 K, and then decreases for higher temperature. Likewise, with the increase of magnetic field, the S_{yx} is monotonously increased, which can be more intuitively reflected in Fig. S2 (ESI†). Under the same magnetic field and temperature, the S_{yx} of polycrystalline NbSb₂ is smaller than that of single-crystalline NbSb₂. For example, the S_{yx} of polycrystalline NbSb₂ is 396 μ V K⁻¹ under 9 T at 21 K, which is 36%

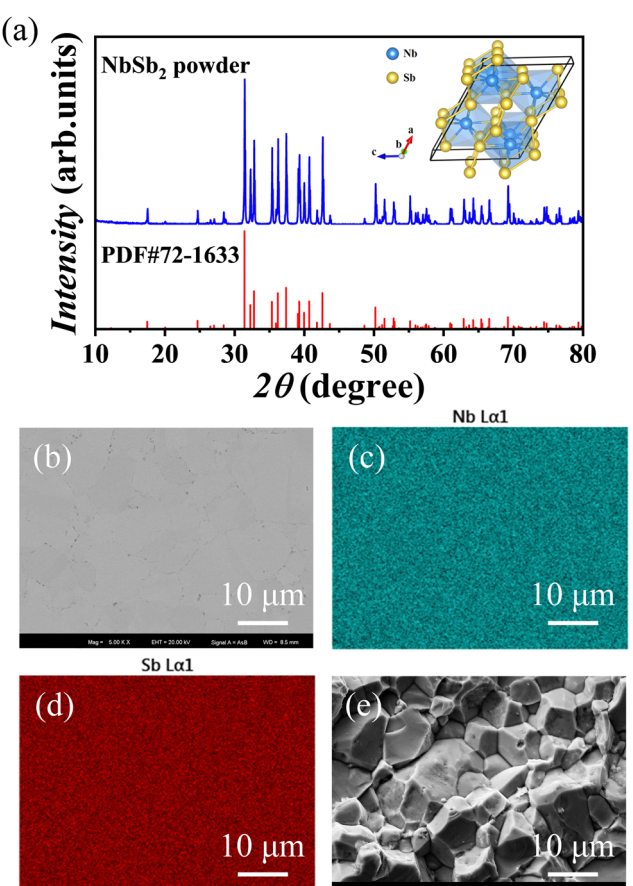


Fig. 2 (a) Powder X-ray diffraction pattern for polycrystalline NbSb₂. The inset shows the crystal structure of NbSb₂. (b) Backscattered electron (BSE) image and (c) and (d) energy dispersive X-ray spectroscopy (EDS) mapping performed on polycrystalline NbSb₂. (e) Cross-section image of fractured polycrystalline NbSb₂.

lower than that of single-crystalline NbSb₂ (616 µV K⁻¹) under the same conditions.²⁰ Thus, the grain boundaries in polycrystalline NbSb₂ lead to decreased S_{vx} .

To obtain the Nernst power factor (PF)_N, a longitudinal electrical conductivity σ_{yy} is required. Under a magnetic field, the motion of the carriers is deflected by the Lorentz force. The motion of the carriers is subject to the influence from other directions. In this case, the σ_{yy} of polycrystalline NbSb₂ can be described as29

$$\sigma_{yy} = \frac{\rho_{xx}}{\rho_{xx}^2 + \rho_{yx}^2}$$
 (1)

where ρ_{xx} is the transverse electrical resistivity and ρ_{yx} is the Hall resistivity. In the absence of magnetic field, the ρ_{xx} of polycrystalline NbSb2 increases with increasing temperature, which is consistent with the semimetal feature of NbSb₂ (Fig. S3a, ESI†). When the magnetic field is applied, the ρ_{xx} is significantly enhanced, particularly below 100 K, indicating the existence of a strong magnetoresistance effect. The ρ_{yx} shown in Fig. S3b (ESI†) is negative over the entire temperature range, indicating that the dominant carriers are electrons in polycrystalline NbSb₂. Under the same magnetic field and temperature, $|\rho_{vx}|$ is much smaller

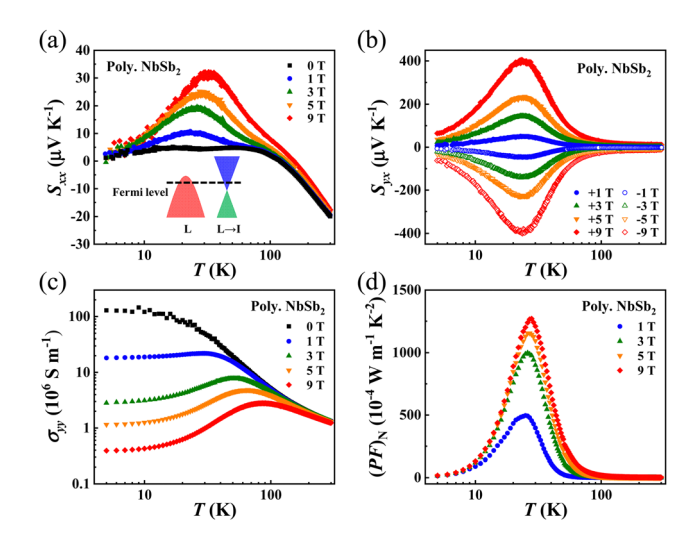


Fig. 3 Temperature dependences of (a) Seebeck thermopower S_{xx} , (b) Nernst thermopower S_{yx} , (c) electrical conductivity σ_{yy} , and (d) Nernst power factor (PF)_N for polycrystalline NbSb₂ under different magnetic fields. The inset in (a) represents the schematics of the band structure of NbSb₂ near the Fermi level.

than ρ_{xx} , indicating that the contributions of electrons and holes in the electrical transports are close. Fig. 3c shows the calculated σ_{yy} for polycrystalline NbSb₂. The temperature-dependence and magnetic field-dependence are similar to those of singlecrystalline NbSb2, but the value is slightly lower than that of single-crystalline NbSb2 under the same magnetic field and temperature. For example, the σ_{yy} of polycrystalline NbSb₂ is 0.65×10^6 S m⁻¹ under 9 T at 21 K, which is 20% lower than that of single-crystalline NbSb₂ (0.81 \times 10⁶ S m⁻¹) under the same conditions.20

Based on the S_{yx} and σ_{yy} , the $(PF)_N$ of polycrystalline NbSb₂ is calculated and plotted in Fig. 3d. Due to the significantly enhanced S_{yx} , the $(PF)_N$ is also greatly increased upon applying magnetic field. When B = 9 T, the peak $(PF)_N$ of polycrystalline $NbSb_2$ is $1269 \times 10^{-4} \text{ W m}^{-1} \text{ K}^{-2}$ at 28 K. Likewise, Fig. S4 (ESI \dagger) shows that the (PF)_N tends to become saturated above 9 T, and thus further increasing the magnetic field will not significantly increase the $(PF)_N$. The peak $(PF)_N$ of polycrystalline NbSb₂ is a very exciting result since it is a record-high value among the polycrystalline thermomagnetic materials (Fig. 1a and Fig. S5, ESI†). Actually, this value is even higher than most singlecrystalline thermomagnetic materials, such as single-crystalline $Bi_{97}Sb_3$, ¹⁰ Cd_3As_2 , ¹⁶ $ZrTe_5$, ¹⁷ $PtSn_4$, ¹⁸ Mg_2Pb , ¹⁹ and $TbPtBi^{28}$ (Fig. 1a and Fig. S5, ESI†), and thermoelectric materials, such as Bi₂Te₃-based alloys, 30,31 AgSbTe₂, 32 TaSiTe₄, 33 and Ag₂S-based materials.34-36

The high (PF)_N of polycrystalline NbSb₂ is mainly contributed by the large S_{yx} . Although the peak S_{yx} of polycrystalline NbSb₂ is lower than the single-crystalline NbSb₂, it is still much higher than most thermomagnetic materials reported before, such as 124 μ V K⁻¹ for polycrystalline NbP under 9 T at 140 K,²³ 127 μV K⁻¹ for polycrystalline Mg₃Bi₂ under 13 T at 13.5 K,²⁴ 125 μ V K⁻¹ for single-crystalline Cd₃As₂ under 3 T at 350 K,¹⁶ 45 μ V K⁻¹ for single-crystalline PtSn₄ under 9 T at 10.3 K, ¹⁸

200 μ V K⁻¹ for single-crystalline Mg₂Pb under 10 T at 30 K,¹⁹ and 225 μ V K⁻¹ for single-crystalline TbPtBi under 14 T at 240 K.²⁸ One main reason for the large S_{yx} is originated from its unsaturated behavior under a high magnetic field. As shown in Fig. S2 (ESI†), the S_{yx} linearly increases with increasing magnetic field, without showing obvious deflection even under 9 T.

When both the electrons and holes take part in electrical transports, the S_{vx} can be expressed as³⁷

$$S_{yx} = \frac{\sigma_{xx}^{e} \sigma_{xx}^{h} (\mu_{e} + \mu_{h}) B}{(\sigma_{xx}^{e} + \sigma_{xx}^{h})^{2}} (S_{xx}^{h} - S_{xx}^{e})$$
 (2)

where $\sigma_{xx}^{\rm e}$ and $\sigma_{xx}^{\rm h}$ are the electrical conductivity contributed by electrons and holes, $S_{xx}^{\rm e}$ and $S_{xx}^{\rm h}$ are the Seebeck thermopower of electrons and holes under the magnetic field, $\mu_{\rm e}$ and $\mu_{\rm h}$ are electron mobility and hole mobility, respectively. $n_{\rm e}$ (or $n_{\rm h}$) and $\mu_{\rm e}$ (or $\mu_{\rm h}$) can be estimated by using the two-carrier model to fit the measured $\rho_{xx}(B)$ and $\rho_{yx}(B)^{38}$

$$\rho_{xx}(B) = \frac{1(n_{\rm h}\mu_{\rm h} + n_{\rm e}\mu_{\rm e}) + (n_{\rm h}\mu_{\rm e} + n_{\rm e}\mu_{\rm h})\mu_{\rm e}\mu_{\rm h}B^2}{{\rm e} (n_{\rm h}\mu_{\rm h} + n_{\rm e}\mu_{\rm e})^2 + (n_{\rm h} - n_{\rm e})^2\mu_{\rm e}^2\mu_{\rm h}^2B^2}$$
(3)

$$\rho_{yx}(B) = \frac{B(n_{\rm h}\mu_{\rm h}^2 - n_{\rm e}\mu_{\rm e}^2) + (n_{\rm h} - n_{\rm e})\mu_{\rm e}^2\mu_{\rm h}^2B^2}{e(n_{\rm h}\mu_{\rm h} + n_{\rm e}\mu_{\rm e})^2 + (n_{\rm h} - n_{\rm e})^2\mu_{\rm e}^2\mu_{\rm h}^2B^2}$$
(4)

Fig. S6 (ESI†) plots the $\rho_{xx}(B)$ and $\rho_{yx}(B)$ for polycrystalline NbSb2 under different temperatures and magnetic field. At low temperatures (below 100 K), $\rho_{xx}(B)$ varies with the magnetic field B by a factor of 2 and $\rho_{yx}(B)$ also significantly deviates off linearity as B increases, which is consistent with the scenario described using eqn (3) and (4) when $\mu B \gg 1$. At high temperatures (above 100 K), the $\rho_{xx}(B)$ and $\rho_{yx}(B)$ exhibit weak magnetic field dependence since the decreased carrier mobility at high temperatures reduces the contribution of the nonlinear terms in eqn (3) and (4). The fitted n_e and n_h of polycrystalline NbSb₂ are very close in the whole temperature range (Fig. 4a). A similar phenomenon was also observed in single-crystalline NbSb₂.²⁰ This is consistent with the band structure of NbSb₂, which shows that the electron pocket and hole pocket near the Fermi level have nearly the same volume. Likewise, the fitted μ_e and μ_h of polycrystalline NbSb2 are also very close in the whole temperature range (Fig. 4b). In this case, eqn (2) can be simplified into

$$S_{yx} = \frac{\bar{\mu}B}{2} \left(S_{xx}^{h} - S_{xx}^{e} \right) \tag{5}$$

where S_{yx} is in proportional to B. This can well explain the observed unsaturated behavior of S_{yx} under a high magnetic field for polycrystalline NbSb₂.

Beyond the high magnetic field, eqn (5) indicates that the high carrier mobility is also necessary for the large S_{yx} . The μ_e and μ_h of polycrystalline NbSb₂ are about 1.7 m² V⁻¹ s⁻¹ and 1.2 m² V⁻¹ s⁻¹ at 5 K, which are quite high values among those for the reported thermomagnetic materials, such as Cd₃As₂ ($\mu_e = 6.5 \text{ m}^2 \text{ V}^{-1} \text{ s}^{-1}$, $\mu_h = 0.5 \text{ m}^2 \text{ V}^{-1} \text{ s}^{-1}$ at 10 K)¹⁶, PtSn₄ ($\mu_e = 7.6 \text{ m}^2 \text{ V}^{-1} \text{ s}^{-1}$, $\mu_h = 7.6 \text{ m}^2 \text{ V}^{-1} \text{ s}^{-1}$ at 10 K),¹⁸ Mg₃Bi₂ ($\mu_e = 0.48 \text{ m}^2 \text{ V}^{-1} \text{ s}^{-1}$, $\mu_h = 0.14 \text{ m}^2 \text{ V}^{-1} \text{ s}^{-1}$ at 15 K),²⁴ and TbPtBi ($\mu_e = 0.3 \text{ m}^2 \text{ V}^{-1} \text{ s}^{-1}$, $\mu_h = 0.3 \text{ m}^2 \text{ V}^{-1} \text{ s}^{-1}$ at 20 K).²⁸ Generally, it is considered that the polycrystals have lower carrier mobility

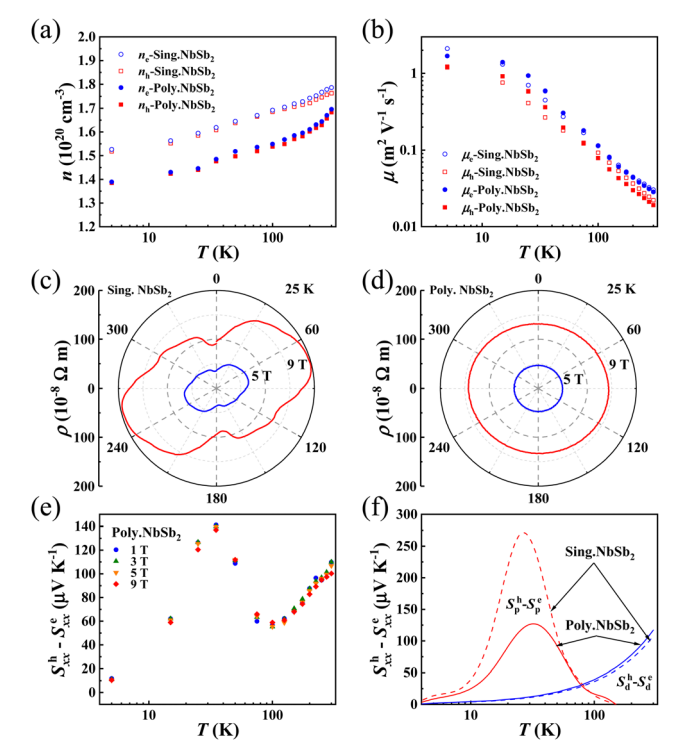


Fig. 4 (a) Carrier concentrations ($n_{\rm e}$ and $n_{\rm h}$) and (b) carrier mobilities ($\mu_{\rm e}$ and $\mu_{\rm h}$) of polycrystalline NbSb₂. Angular dependence of electrical resistivity ρ measured (c) along the b-axis of single-crystalline NbSb₂ and (d) the direction perpendicular the sintering pressure of polycrystalline NbSb₂ under 5 T and 9 T at 25 K. (e) Temperature dependence of the difference of Seebeck thermopower of electrons and holes ($S_{xx}^h - S_{xx}^e$) for polycrystalline NbSb₂ under different magnetic fields. (f) The difference of Seebeck thermopower of electrons and holes related to the charge carrier diffusion processes ($S_{\rm d}^e - S_{\rm d}^h$) and phonons ($S_{\rm p}^e - S_{\rm p}^h$) of polycrystalline and single-crystalline NbSb₂ at 5 T, respectively. The data of single-crystalline NbSb₂ are included in (a), (b), (e), and (f) for comparison.

than the single crystals due to the additional grain boundary scattering to carriers. Interestingly, herein the polycrystalline NbSb₂ have similar μ_e and μ_h with the single-crystalline NbSb₂ in the bc-plane. This abnormal phenomenon is related to the anisotropic transport properties of single crystalline NbSb2 at low temperatures. Herein, we measured the angular dependence of the resistivity ρ of single-crystalline NbSb₂ under a magnetic field to investigate the anisotropy. As shown in Fig. S7a and b (ESI†), for the single-crystalline NbSb₂, the angle between the magnetic field and the normal to the bc-plane is noted as θ . When $\theta = 0^{\circ}$, the position of the magnetic field is perpendicular to the bc-plane. This is the condition used to measure the carrier mobility of single-crystalline NbSb2 in a previous work.²⁰ For the polycrystalline NbSb₂, the angle between the magnetic field and the direction of the sintering pressure is noted as θ . When $\theta = 0^{\circ}$, the position of the magnetic field is parallel to the direction of the sintering pressure. In the case that the carrier mobility is isotropic, the measured angle dependence of ρ should possess a circle shape.

As shown in Fig. 4c, the measured angle dependence of ρ for single-crystalline NbSb₂ under 5 T or 9 T at 25 K has a typical two-fold rotational symmetry, which is similar to the crystal

structure projection of NbSb2 in the ac-plane (the inset in Fig. 2a). Under 9 T, the ρ at $\theta = 0^{\circ}$ is just $94 \times 10^{-8} \Omega$ m, which is about 47% that at $\theta = 75^{\circ}$ or 255° ($198 \times 10^{-8} \Omega$ m). Since the carrier concentration is isotropic, the anisotropic ρ indicates that the carrier mobility of single-crystalline NbSb2 varies considerably in the [010] crystal zone and that in the bc-plane is much lower than those in other planes. In contrast, the measured angle dependence of ρ in polycrystalline NbSb₂ at 25 K is nearly a circle (Fig. 4d). At 9 T, the maximum ρ (143 \times $10^{-8} \Omega$ m at around $\theta = 94^{\circ}$ or 274°) is just about 1.09 times the minimum ρ (131 \times 10⁻⁸ Ω m at around θ = 5° or 185°). This indicates the carrier mobility in the polycrystalline NbSb2 has weak anisotropy, which is consistent with the randomly distributed grains shown in Fig. 2e. Thus, the measured carrier mobility of polycrystalline NbSb2 should simultaneously include the contributions from all planes and grain boundaries. This can explain why the polycrystalline NbSb₂ has a high carrier mobility comparable with the single-crystalline NbSb2 in the *bc*-plane.

Although the polycrystalline NbSb2 has similar carrier mobilities to the single-crystalline NbSb₂, it has lower $(S_{xx}^{h} - S_{xx}^{e})$. As shown in Fig. 4e, under 9 T, the peak $(S_{xx}^h - S_{xx}^e)$ of polycrystalline NbSb₂ is about 137 μ V K⁻¹, which is about 57% that of singlecrystalline NbSb₂. ²⁰ The $(S_{xx}^{h} - S_{xx}^{e})$ includes two parts, termed as the $(S_d^h - S_d^e)$ related to the diffusion process of charge carriers and the $(S_p^h - S_p^e)$ related to the phonon-drag effect.³⁹ Fig. 4f shows the $(S_{\rm d}^{\rm h}-S_{\rm d}^{\rm e})$ and $(S_{\rm p}^{\rm h}-S_{\rm p}^{\rm e})$ of the polycrystalline NbSb₂, with the calculation details shown in the Supplementary Information. The former is comparable with that of single-crystalline NbSb₂, which is consistent with their similar carrier concentrations shown in Fig. 4a. However, the latter is much lower than that of singlecrystalline NbSb₂, indicating the weaker phonon-drag effect in polycrystalline NbSb₂. The phonon-drag effect is caused by the interaction between the long-wavelength acoustic phonons and the carriers on the Fermi surface.8 In polycrystals, 40,41 due to the grain boundary scattering, the relaxation time of the participating long-wavelength phonons is reduced, leading to the suppressed phonon-drag effect.

Fig. 5a and b show the temperature dependence and magnetic field dependence of thermal conductivity κ_{xx} for polycrystalline NbSb₂. As the temperature increases, the κ_{xx} first increases, reaching a peak around 35 K, and then decreases at higher temperature. Upon applying a magnetic field, κ_{xx} shows obvious reduction, especially below 30 K (Fig. 5a). This is caused by the suppressed carrier thermal conductivity κ_c under magnetic field. The κ_c and lattice thermal conductivity κ_l can be obtained by fitting the measured κ_{xx} according to an empirical formula 18,42,43

$$\kappa_{xx}(B,T) = \kappa_{l}(T) + \frac{\kappa_{c}(0,T)}{1 + \eta B^{s}}$$
 (6)

where η and s are the two factors related to the thermal mobility and scattering mechanism, respectively. As shown in Fig. 5b, the fitting results agree well with the experimental data. The fitting parameters are shown in Table S1 (ESI†). The fitted κ_1 values of polycrystalline NbSb₂ are plotted in the inset of Fig. 5a. The peak κ_1 , appearing around 50 K, is 57.1 W m⁻¹ K⁻¹, which is slightly lower

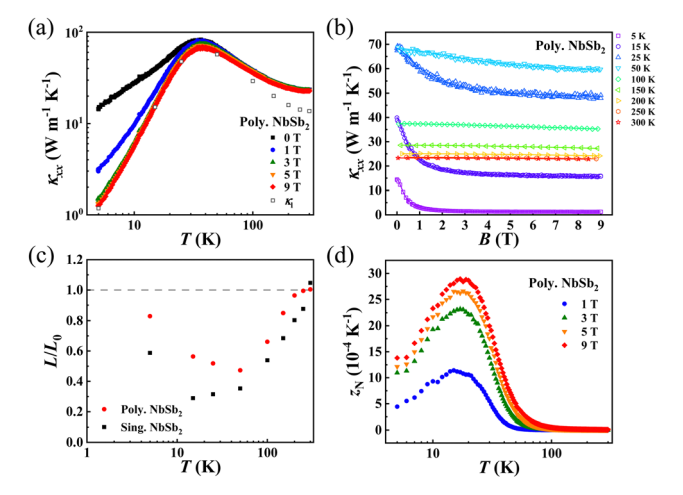


Fig. 5 (a) Temperature dependence of thermal conductivity κ_{xx} and lattice thermal conductivity κ_1 under different magnetic fields for polycrystalline NbSb₂. (b) Magnetic field dependence of thermal conductivity κ_{xx} at different temperatures. The symbols are experimental data and the lines are the fitting curves. (c) The ratio of Lorentz number and the Sommerfeld value (L/L_0) for polycrystalline NbSb₂. (d) Temperature dependence of the Nernst figure-of-merit z_N for polycrystalline NbSb₂ under different magnetic fields. The data of single-crystalline NbSb2 are included in (c) and (d) for comparison.²⁰

than that of the single-crystalline NbSb2 along the b-axis $(64.3 \text{ W m}^{-1} \text{ K}^{-1} \text{ at } 25 \text{ K}).^{20} \text{ At } 300 \text{ K}, \text{ the } \kappa_{xx} \text{ is } 23.5 \text{ W}^{-1} \text{ m}^{-1} \text{ K}^{-1},$ which is still much higher than the state-of-the-art materials for Peltier refrigeration around room temperature, such as 0.7 W m^{-1} K $^{-1}$ for Bi₂Te₃, 31 0.7 W m^{-1} K $^{-1}$ for Mg₃Bi₂, 5 and 0.34 W m⁻¹ K⁻¹ for Ag₂Se.⁴⁴ Under a high magnetic field, such as 9 T, κ_c is already very low (Fig. S8, ESI†), and κ_1 dominates the measured κ_{xx} . Thus, reducing the overhigh κ_1 is an important task for the investigation of NbSb₂ in the future.

Similar to most topological semimetal materials, the polycrystalline NbSb₂ also exhibits the abnormal Lorenz number L deviating off the classic Sommerfeld value L_0 below room temperature. Based on the fitted κ_c , the L can be calculated by using the Wiedemann–Franz law $L = \kappa_c/(\sigma_{xx}T)$. Fig. 5c plots the temperature dependence of L/L_0 for polycrystalline NbSb₂. With increasing temperature, the L/L_0 firstly decreases, reaching a minimum around 50 K, and then increases at higher temperature. The violation of the Wiedemann-Franz law at intermediate temperature range might be caused by the inelastic scattering, 45-47 while the upturn of L/L_0 below and above 50 K might be caused by the changed carrier scattering mechanism to the elastic scattering from the impurities and elastic electron-phonon scattering, respectively. Likewise, the L/L_0 of polycrystalline NbSb₂ is larger than that of single-crystalline NbSb₂, which might be caused by the dilution of inelastic scattering by grain boundary scattering.

Based on the S_{yx} , σ_{yy} , and κ_{xx} , the Nernst figure-of-merit $z_{\rm N} \ (= S_{yx}^2 \sigma_{yy}/\kappa_{xx})$ is calculated for polycrystalline NbSb₂. The detailed derivation process of z_N can be found in the Supplementary Information. Similar to the figure-of-merit z for thermoelectric materials, the z_N is also a parameter that is independent of the material's geometric factors. As shown in Fig. 5d, the z_N increases with increasing temperature, reaches a

maximum around 18 K, and then decreases at higher temperature. Likewise, Fig. S9 (ESI†) shows that the $z_{\rm N}$ tends to saturate above 9 T, thus further increasing the magnetic field will not significantly increase $z_{\rm N}$. The peak $z_{\rm N}$ of polycrystalline NbSb₂ is already much higher than all the polycrystalline thermomagnetic materials reported before (Fig. 1b and Fig. S10, ESI†), such as 0.93×10^{-4} K⁻¹ for polycrystalline NbP under 9 T at 220 K²³ and 14.6×10^{-4} K⁻¹ for polycrystalline Mn-doped Mg₃Bi₂ under 14 T at 14 K.²⁵ Actually, this value is also higher than those of many single-crystalline thermomagnetic materials reported before, such as 8×10^{-4} K⁻¹ for PtSn₄ under 9 T at 10.3 K.¹⁸ If the overhigh $\kappa_{\rm I}$ can be reduced without deteriorating the electrical transport properties, a higher $z_{\rm N}$ can be expected.

Based on the physical properties of polycrystalline NbSb₂, the maximum temperature difference ($\Delta T_{\rm max}$) and maximum specific heat pumping power ($P_{\rm max}$) of a rectangular Ettingshausen refrigerator made of polycrystalline NbSb₂ can be estimated. ^{8,19} Under B=9 T and $T_{\rm c}=30$ K, the $\Delta T_{\rm max}$ of the NbSb₂-based Ettingshausen refrigerator with the thickness of 1 mm along the heat flow direction is about 0.9 K and the theoretical $P_{\rm max}$ is about 6.5 W g⁻¹. The latter value is much higher than the compression refrigerator with gas refrigerants (e.g. $P_{\rm max}=0.05$ W g⁻¹ for He at 5 K, 0.12 W g⁻¹ for H₂ at 26 K, and 1.01 W g⁻¹ for N₂ at 93 K). ¹⁹ Thus, the polycrystalline NbSb₂ has a great potential to be used for Ettingshausen refrigeration.

Conclusions

In summary, we found that the polycrystalline NbSb₂ has an unsaturated Nernst thermopower S_{yx} of 396 μ V K⁻¹ under 9 T at 21 K and a giant Nernst power factor $(PF)_N$ of \sim 1269 \times 10⁻⁴ W m⁻¹ K⁻² under 9 T at 28 K. The latter is almost an order of magnitude larger than the reported $(PF)_N$ of other polycrystalline thermomagnetic materials. The z_N of polycrystalline NbSb₂ is 28.5 \times 10⁻⁴ K⁻¹ under 9 T at 18 K, which is also a record-high value among the reported polycrystalline thermomagnetic materials. The superior $(PF)_N$ and z_N are attributed to the nearly identical electron and hole concentrations near the Fermi level, ultrahigh mobilities close to 1 m² V⁻¹ s⁻¹, and the strong phonon-drag effect in low temperature ranges. Combining the low-cost and time-saving fabrication process, polycrystalline NbSb₂ is a very competitive candidate material for Ettingshausen refrigeration.

Experimental section

Sample synthesis

Polycrystalline NbSb₂ was synthesized *via* the solid-stated reaction and spark plasma sintering technique. The niobium powder (alfa, 99.99%) and antimony shot (alfa, 99.9999%) were encapsulated in a vacuum quartz tube and reacted at 1023 K for 48 h. The obtained product was ground into fine powders, loaded into a graphite mold and compacted by spark plasma sintering (SPS, SPS-725, Sojitz, Japan) in a vacuum. The sintering

temperature was 1123 K and the sintering pressure was 65 MPa. The holding time at 1123 K is 10 min. The relative density of the sintered product was 98%.

Sample characterization

The phase composition was characterized by X-ray diffraction (XRD, D/max-2550 V, Rigaku, Japan). The elemental distribution was characterized by scanning electron microscopy (SEM, ZEISS supra-55, Germany) with energy dispersive X-ray spectroscopy (EDS, Oxford, UK). The bulk sample was cut into the strips of about $8 \times 2 \times 2 \text{ mm}^3$ and $8 \times 2 \times 1 \text{ mm}^3$ for electrical and thermal transport measurements under the magnetic field, respectively. All measurements were carried out on a physical property measurement system (PPMS, Quantum design, USA). The electrical resistivity and Hall resistivity were measured using a four-probe method and five-probe method, respectively. The Seebeck thermopower and Nernst thermopower were measured using the four-probe method on a standard thermal transport option (TTO) platform and a modified one, respectively. The details can be found in ref. 20. The S_{yx} data used to calculate Nernst power factor and Nernst figure-of-merit are obtained as $S_{yx} = [S_{yx} (+B) - S_{yx} (-B)]/2$ to eliminate the effects of contact misalignment.

Author contributions

P. L., P. Q., and X. S. designed the work. P. L. synthesized the samples and performed the transport property measurements with the help of J. X., and P. L. and T. D. analyzed the transport properties. L. C. provided helpful discussion. P. L., P. Q., and X. S. analyzed the data and wrote the manuscript.

Conflicts of interest

The authors declare no competing financial interests.

Acknowledgements

This work was supported by the National Natural Science Foundation of China (grants 52122213 and 91963208), the Shanghai Pilot Program for Basic Research-Chinese Academy of Science, Shanghai Branch (JCYJ-SHFY-2022-002), and the Shanghai Government (20JC1415100).

Notes and references

- 1 J. Chan, T. P. M. Alegre, A. H. Safavi-Naeini, J. T. Hill, A. Krause, S. Gröblacher, M. Aspelmeyer and O. Painter, *Nature*, 2011, 478, 89–92.
- 2 C. Coats, J. S. Rogers and P. McIntyre, *IEEE Trans. Appl. Supercond.*, 2023, 33, 1–5.
- 3 Y. Han and A. Zhang, Sci. Rep., 2022, 12, 2349.
- 4 J. Mao, G. Chen and Z. Ren, Nat. Mater., 2021, 20, 454-461.
- 5 J. Mao, H. Zhu, Z. Ding, Z. Liu, A. Gamage Geethal, G. Chen and Z. Ren, *Science*, 2019, 365, 495–498.

- 6 Y. Qin, B. Qin, D. Wang, C. Chang and L. Zhao, Energy Environ. Sci., 2022, 15, 4527-4541.
- 7 Y. Zheng, X. Han, J. Yang, Y. Jing, X. Chen, Q. Li, T. Zhang, G. Li, H. Zhu, H. Zhao, G. J. Snyder and K. Zhang, Energy Environ. Sci., 2022, 15, 2374-2385.
- 8 H. J. Goldsmid, Thermoelectric Refrigeration, Plenum Press, Wembley, 1964.
- 9 H. J. Goldsmid, in CRC Handbook of Thermoelectrics, ed. D. M. Rowe, CRC Press LLC, Boca Raton, 1995, ch. 8, pp. 73-74.
- 10 K. F. Cuff, R. B. Horst, J. L. Weaver, S. R. Hawkins, C. F. Kooi and G. M. Enslow, Appl. Phys. Lett., 1963, 2, 145-146.
- 11 W. M. Yim and A. Amith, Solid-State Electron., 1972, 15, 1141-1165.
- 12 B. Madon, J. E. Wegrowe, H. J. Drouhin, X. Liu, J. Furdyna and G. A. Khodaparast, J. Appl. Phys., 2016, 119, 025701.
- 13 C. Fu, Y. Sun and C. Felser, APL Mater., 2020, 8, 040913.
- 14 X. Li, Z. Zhu and K. Behnia, Adv. Mater., 2021, 33, 2100751.
- 15 K. Behnia and H. Aubin, Rep. Prog. Phys., 2016, 79, 046502.
- 16 J. Xiang, S. Hu, M. Lyu, W. Zhu, C. Ma, Z. Chen, F. Steglich, G. Chen and P. Sun, Sci. China: Phys., Mech. Astron., 2019, 63, 237011.
- 17 P. Wang, C. Cho, F. Tang, P. Wang, W. Zhang, M. He, G. Gu, X. Wu, Y. Shao and L. Zhang, Phys. Rev. B, 2021, 103, 045203.
- 18 C. Fu, S. N. Guin, T. Scaffidi, Y. Sun, R. Saha, S. J. Watzman, A. K. Srivastava, G. Li, W. Schnelle, S. S. P. Parkin, C. Felser and J. Gooth, Research, 2020, 2020, 4643507.
- 19 Z. Chen, X. Zhang, J. Ren, Z. Zeng, Y. Chen, J. He, L. Chen and Y. Pei, Nat. Commun., 2021, 12, 3837.
- 20 P. Li, P. Qiu, Q. Xu, J. Luo, Y. Xiong, J. Xiao, N. Aryal, Q. Li, L. Chen and X. Shi, Nat. Commun., 2022, 13, 7612.
- 21 Y. Pan, B. He, T. Helm, D. Chen, W. Schnelle and C. Felser, Nat. Commun., 2022, 13, 3909.
- 22 C. Fu, S. N. Guin, S. J. Watzman, G. Li, E. Liu, N. Kumar, V. Süβ, W. Schnelle, G. Auffermann, C. Shekhar, Y. Sun, J. Gooth and C. Felser, Energy Environ. Sci., 2018, 11, 2813-2820.
- 23 W. Liu, Z. Wang, J. Wang, H. Bai, Z. Li, J. Sun, X. Zhou, J. Luo, W. Wang, C. Zhang, J. Wu, Y. Sun, Z. Zhu, Q. Zhang and X. Tang, Adv. Funct. Mater., 2022, 32, 2202143.
- 24 T. Feng, P. Wang, Z. Han, L. Zhou, W. Zhang, Q. Liu and W. Liu, Adv. Mater., 2022, 34, 2200931.
- 25 T. Feng, P. Wang, Z. Han, L. Zhou, Z. Wang, W. Zhang, Q. Liu and W. Liu, Energy Environ. Sci., 2023, 16, 1560-1568.
- 26 S. J. Watzman, T. M. McCormick, C. Shekhar, S.-C. Wu, Y. Sun, A. Prakash, C. Felser, N. Trivedi and J. P. Heremans, Phys. Rev. B, 2018, 97, 161404(R).
- 27 C. Shekhar, A. K. Nayak, Y. Sun, M. Schmidt, M. Nicklas, I. Leermakers, U. Zeitler, Y. Skourski, J. Wosnitza, Z. Liu, Y. Chen, W. Schnelle, H. Borrmann, Y. Grin, C. Felser and B. Yan, Nat. Phys., 2015, 11, 645-649.

- 28 H. Wang, Z. Zhou, J. Ying, Z. Xiang, R. Wang, A. Wang, Y. Chai, M. He, X. Lu, G. Han, Y. Pan, G. Wang, X. Zhou and X. Chen, Adv. Mater., 2023, 35, 2206941.
- 29 R. T. Delves, Rep. Prog. Phys., 1965, 28, 249-289.
- 30 X. Liu, T. Xing, P. Qiu, T. Deng, P. Li, X. Li, X. Li and X. Shi, *J. Materiomics*, 2023, **9**, 345–352.
- 31 R. Deng, X. Su, Z. Zheng, W. Liu, Y. Yan, Q. Zhang, V. P. Dravid, C. Uher, M. G. Kanatzidis and X. Tang, Sci. Adv., 2018, 4, eaar5606.
- 32 Y. Wu, P. Qiu, Y. Yu, Y. Xiong, T. Deng, O. Cojocaru-Mirédin, M. Wuttig, X. Shi and L. Chen, J. Materiomics, 2022, 8, 1095-1103.
- 33 Q. Xu, C. Ming, T. Xing, P. Qiu, J. Xiao, X. Shi and L. Chen, Mater. Today Phys., 2021, 19, 100417.
- 34 Z. Gao, Q. Yang, P. Qiu, T.-R. Wei, S. Yang, J. Xiao, L. Chen and X. Shi, Adv. Energy Mater., 2021, 11, 2100883.
- 35 Q. Yang, S. Yang, P. Qiu, L. Peng, T.-R. Wei, Z. Zhang, X. Shi and L. Chen, Science, 2022, 377, 854-858.
- 36 M. Jin, X. Bai, R. Zhang, L. Zhou and R. Li, J. Inorg. Mater., 2021, 37, 101-106.
- 37 R. T. Delves, Br. J. Appl. Phys., 1964, 15, 105-106.
- 38 L. Guo, Y. K. Liu, G. Y. Gao, Y. Y. Huang, H. Gao, L. Chen, W. Zhao, W. Ren, S. Y. Li, X. G. Li, S. Dong and R. K. Zheng, J. Appl. Phys., 2018, 123, 155103.
- 39 F. J. Blatt, P. A. Schroeder, C. L. Foiles and D. Greig, Thermoelectric power of metals, Plenum Press, New York and London, 1976.
- 40 J. Zhou, B. Liao, B. Qiu, S. Huberman, K. Esfarjani, M. S. Dresselhaus and G. Chen, Proc. Natl. Acad. Sci. U. S. A., 2015, 112, 14777-14782.
- 41 M. Pokharel, H. Zhao, K. Lukas, Z. Ren, C. Opeil and B. Mihaila, MRS Commun., 2013, 3, 31-36.
- 42 R. Ocaña and P. Esquinazi, Phys. Rev. B, 2002, 66, 064525.
- 43 F. Han, N. Andrejevic, T. Nguyen, V. Kozii, Q. T. Nguyen, T. Hogan, Z. Ding, R. Pablo-Pedro, S. Parjan, B. Skinner, A. Alatas, E. Alp, S. Chi, J. Fernandez-Baca, S. Huang, L. Fu and M. Li, Nat. Commun., 2020, 11, 6167.
- 44 J. Liang, P. Qiu, Y. Zhu, H. Huang, Z. Gao, Z. Zhang, X. Shi and L. Chen, Research, 2020, 2020, 6591981.
- 45 J. Gooth, F. Menges, N. Kumar, V. Subeta, C. Shekhar, Y. Sun, U. Drechsler, R. Zierold, C. Felser and B. Gotsmann, Nat. Commun., 2018, 9, 4093.
- 46 A. Jaoui, B. Fauqué, C. W. Rischau, A. Subedi, C. Fu, J. Gooth, N. Kumar, V. Süß, D. L. Maslov, C. Felser and K. Behnia, npj Quantum Mater., 2018, 3, 64.
- 47 N. Kumar, Y. Sun, M. Nicklas, S. J. Watzman, O. Young, I. Leermakers, J. Hornung, J. Klotz, J. Gooth, K. Manna, V. Süß, S. N. Guin, T. Förster, M. Schmidt, L. Muechler, B. Yan, P. Werner, W. Schnelle, U. Zeitler, J. Wosnitza, S. S. P. Parkin, C. Felser and C. Shekhar, Nat. Commun., 2019, 10, 2475.